Journal of Materials Chemistry A

ROYAL SOCIETY OF CHEMISTRY

COMMUNICATION

View Article Online
View Journal

Cite this: DOI: 10.1039/d6ta00836d

Received 28th January 2026
Accepted 8th April 2026

DOI: 10.1039/d6ta00836d

rsc.li/materials-a

Phosphorus-doped hard carbon derived from waste PET bottles as a superior anode material for lithium-ion batteries

Dossym Yeskozha,[a] Aisha Zhanaikhan,[ab] Aizhuz Sarsengaliyeva,[ab] Yergali Mustafa,[c] Zumabay Bakenov,[ade] Aliya Mukanova *[ad] and Arailym Nurpeissova *[ad]

Plastic pollution remains a significant environmental challenge, with polyethylene terephthalate (PET) bottles contributing heavily due to their durability and limited degradability. Upcycling PET into functional carbon materials provides a sustainable alternative to conventional recycling routes, which often generate microplastics. Owing to its high carbon content and abundant ester groups, PET serves as an excellent precursor for hard carbon (HC), suitable for use in electrochemical energy-storage applications. In this work, waste PET bottles are upcycled into phosphorus-doped hard carbon (P-HC) through a single-step pyrolysis process using orthophosphoric acid (H_3PO_4). The resulting P-HC demonstrates markedly enhanced electrochemical performance compared with undoped PET-derived carbon. The sample prepared with 3 mL of phosphoric acid exhibits the most favorable properties, delivering a high reversible capacity of 765 mAh g^{-1} after 100 cycles at 0.2 A g^{-1} and 531 mAh g^{-1} after 200 cycles at 2 A g^{-1}. These improvements are attributed to increased interlayer spacing, higher surface area, greater structural disorder, and improved electronic conductivity induced by phosphorus incorporation. The study demonstrates a sustainable route for converting PET waste into high-performance anode materials for lithium-ion batteries (LIBs), addressing both environmental concerns and the growing demand for efficient energy-storage technologies.

1. Introduction

The modern world faces a critical challenge with plastic pollution, necessitating innovative solutions for sustainable management.[1,2] One promising approach is the upcycling of plastic materials into more valuable products, thereby reducing the generation of microplastics associated with conventional recycling.[3–6] Among various plastics, polyethylene terephthalate (PET) from single-use beverage bottles has been identified as a potential raw material for the production of hard carbon (HC) anodes in lithium-ion batteries (LIBs) due to its high carbon content and abundance of ester bonds.[7–11] PET, predominantly used in single-serve beverage packaging, represents a substantial portion of global solid waste, posing environmental challenges due to its non-biodegradable nature.[12,13] Concurrently, the demand for efficient energy storage systems continues to increase with the rapid development of portable electronics and electric vehicles, stimulating extensive research on advanced carbon-based anode materials with improved ion transport kinetics.[14,15]

The intersection of these two critical issues – plastic waste management and energy storage innovation – presents a unique opportunity for scientific exploration and technological advancement. Despite being a promising precursor, bare PET-derived HC exhibits poor reversible capacity at high current rates and low initial coulombic efficiency (CE). For example, Mirjalili *et al.* reported that PET-based anodes obtained by carbonization of electrospun products showed good electrochemical stability but still suffered from limited capacity in LIBs.[16–19] These findings highlight the need for further modifications and structural adjustments to achieve high-performance anode materials.

One of the solutions to overcome these limitations is to introduce heteroatoms into the carbon framework to further improve the electrochemical performance of the HC. Thus, P-doping of hard carbon is regarded as an effective strategy to improve alkali-ion storage because it can enlarge the interlayer spacing, modify the electronic environment, and promote ion adsorption/diffusion within the carbon framework.[20–23] For instance, Wu *et al.* synthesized phosphorus-doped HC nanofibers using electrospinning, achieving a reversible capacity of 288 mAh g^{-1} at 50 mA g^{-1}, demonstrating good cycling stability

[a]Institute of Batteries LLP, 53 Kabanbay Batyr Ave., Astana, 010000, Kazakhstan. E-mail: arailym.nurpeissova@nu.edu.kz
[b]L.N. Gumilyov Eurasian National University, 2 Satpayeva St., Astana, 010000, Kazakhstan
[c]Almaty University of Power Engineering and Telecommunications, 126 Baitursynov St., Almaty, 050057, Kazakhstan
[d]Institute of New Materials and Energy Technologies PI, 53 Kabanbay Batyr Ave., Astana 010000, Kazakhstan
[e]Nazarbayev University, 53 Kabanbay Batyr Ave., Astana 010000, Kazakhstan

with 87.8% retention after 200 cycles.[24] Similarly, Wang *et al.* prepared phosphorus-doped hollow carbon nanorods (P-HCNs) with a phosphorus content of 7.5 at%, achieving a capacity of 260 mAh g^{-1} after 500 cycles at 1 A g^{-1}. Their research highlighted the strong ion absorption ability of P–C and P–O bonds, which contributed to the improved electrochemical performance.[25]

Similar effects have been observed in N/P co-doped carbon systems, where phosphorus incorporation induces structural distortion of the carbon framework and promotes the formation of active adsorption sites for alkali ions.[26] In addition to heteroatom doping, advanced structural engineering strategies have been widely explored to improve the electrochemical stability of high-capacity anode materials in alkali-ion batteries. For example, Lin *et al.* developed a dual-carbon confinement architecture in which SnO_2 nanocrystals are anchored within an inner CNT network and encapsulated by an outer N-doped carbon shell, effectively suppressing volume expansion and improving electron transport in SIB anodes.[27] Building on this approach, Zhao *et al.* extended the dual-carbon confinement strategy to WS_2-based hierarchical structures (HC@WS_2@NC), where the hard carbon core and N-doped carbon shell simultaneously stabilize the active material and accelerate charge transfer.[28] Furthermore, constructing MoS_2/WS_2 heterostructures within dual carbon layers (HC@MoS_2/WS_2@NC) introduces a built-in interfacial electric field that further modulates ion transport kinetics and mechanical buffering during Na^+ insertion/extraction.[29]

However, structural instability of the doped HC structure is a concern, as excessive phosphorus doping can lead to over-expansion of the carbon matrix, weakening its mechanical integrity and leading to faster degradation during cycling.[30–32] P-doping can also cause irreversible capacity loss, especially during the initial charge–discharge cycles, as defects introduced by doping may lead to increased reactivity with the electrolyte.[31] Moreover, increased side reactions between the doped material and the electrolyte, particularly at higher doping levels, can degrade the long-term stability of the battery.[33] Thus, precise control over the amount of P-doping agent is crucial for effective phosphorus doping of the anode material.

Beyond structural instability, low initial coulombic efficiency (ICE) represents a persistent challenge for hard carbon anodes derived from oxygen-rich precursors such as PET, owing to irreversible lithium consumption during SEI formation and reactions with surface functional groups. Several mitigation strategies have been identified in the literature. Electrolyte additives such as fluoroethylene carbonate (FEC) or vinylene carbonate (VC) promote the rapid formation of a thin, inorganic-rich SEI and suppress continuous electrolyte decomposition on highly porous carbon surfaces.[34] Pre-lithiation approaches—chemical, electrochemical, or *via* sacrificial Li-rich additives—can compensate for the initial irreversible Li loss associated with deep pore trapping and defect-site filling.[35,36] Additionally, surface engineering strategies, including mild post-annealing to reduce excessive microporosity and reactive oxygen groups, as well as the application of artificial interphases *via* ALD- or MLD-deposited oxide/phosphate layers, have been shown to passivate reactive surface sites and homogenize SEI formation on high-surface-area carbon anodes.[37] These considerations motivate the careful optimization of P-doping level demonstrated in the present work.

In this work, we demonstrate a simple yet effective strategy for phosphorus doping of PET through one-step carbonization with H_3PO_4. The doping level was precisely adjusted by varying the amount of H_3PO_4 added during PET dissolution, ensuring controlled phosphorus incorporation without additional complex processing. This approach enables direct upcycling of PET into functional hard carbon, yielding materials with enhanced conductivity, enlarged interlayer spacing, and improved porosity. The optimally doped sample delivers high reversible capacity, excellent rate capability, and stable cycling, significantly outperforming the non-doped counterpart.

2. Experimental

2.1. Materials preparation

Post-consumer Coca-Cola bottles were collected for the research. Dichloromethane (DCM) and trifluoroacetic acid (TFA), obtained from Sigma-Aldrich, were used in the experimental procedures. Orthophosphoric acid (87%, hydrous) was procured from Sigma-Aldrich for use in the experiment as a P-doping precursor. To obtain HC, the label, cap, and cap ring were removed from the post-consumer PET bottles. The bottles were then cut into ~2 × 2 mm fragments, washed sequentially with deionized water and ethanol, and dried in a vacuum oven at 60 °C for 24 h. Subsequently, 2 g of the prepared PET fragments were dispersed in a DCM/TFA solvent system (7 : 3 vol/vol) at a polymer loading of 20 wt%. Orthophosphoric acid in different amounts (1–5 mL) was added to the solution, while a control sample was prepared without the acid. Depending on the amount of H_3PO_4 added, the samples were denoted as 1P-PET, 2P-PET, 3P-PET, and 5P-PET, corresponding to 1 mL, 2 mL, 3 mL, and 5 mL of acid, respectively. A control sample without H_3PO_4 was denoted as 0P-PET. All mixtures were stirred at room temperature for 4 h using a magnetic stirrer at 100 rpm.

The air-dried samples were cut and placed in ceramic crucibles, which were then positioned within a quartz tube at 750 °C (Across International) under N_2 atmosphere. The calcination process involves two steps: (1) heating to 250 °C at a rate of 5 °C min^{-1} for 2 hours, and (2) maintaining a working temperature of 750 °C for 2 hours. After carbonization, the obtained carbon materials were denoted as 0P-HC, 1P-HC, 2P-HC, 3P-HC, and 5P-HC, corresponding to the precursor samples 0P-PET, 1P-PET, 2P-PET, 3P-PET, and 5P-PET, respectively. The entire procedure for obtaining P-doped HC (P-HC) is depicted in Fig. 1.

2.2. Materials characterization

Thermogravimetric analysis (TGA) of dried plastic samples was conducted using a Netzsch DSC-TGA with IR coupling, under a nitrogen atmosphere (99.9% purity) at a heating rate of 5 °C min^{-1}. A powder X-ray diffractometer (XRD, MiniFlex

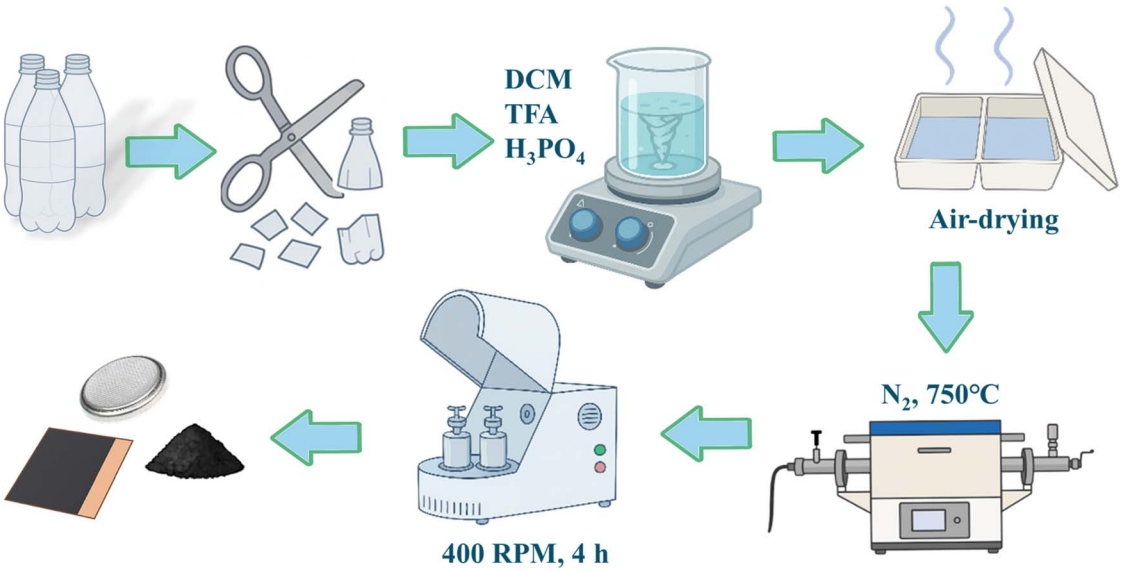

Fig. 1 Schematic illustration of the PET carbonization process.

Benchtop, with Ni-filtered Cu Kα radiation) was used to determine the structure of the carbon samples in the range of 10–80° at a scanning rate of 5° min^{-1}. Scanning electron microscopy (SEM, ZEISS Crossbeam 540) and high-resolution transmission electron microscopy (HRTEM, FEI TalosF200S Super) were used to observe and analyze its microstructure. Raman spectroscopy

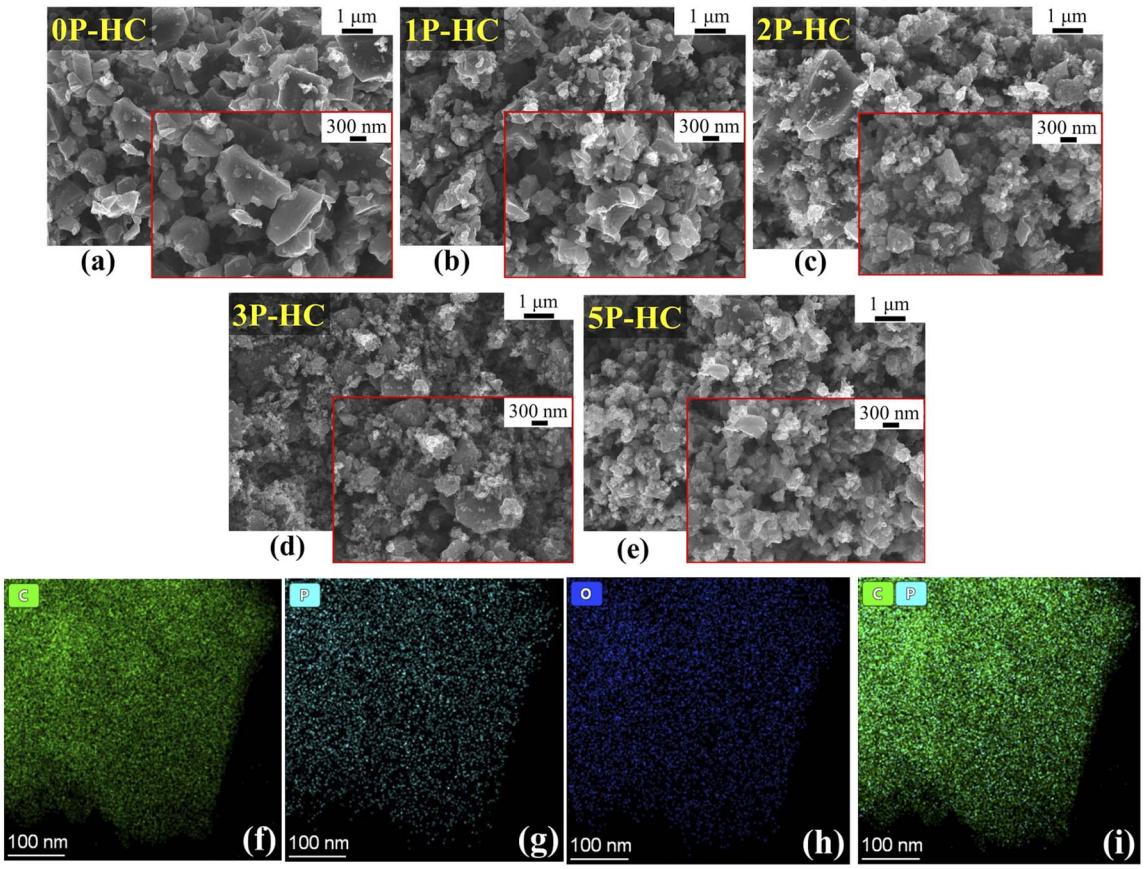

Fig. 2 SEM images of the (a) non-doped; (b–e) P-doped HC-samples. The EDS elemental mapping of (f) C, (g) P, (h) O, (i) C and P for the 3P-HC sample.

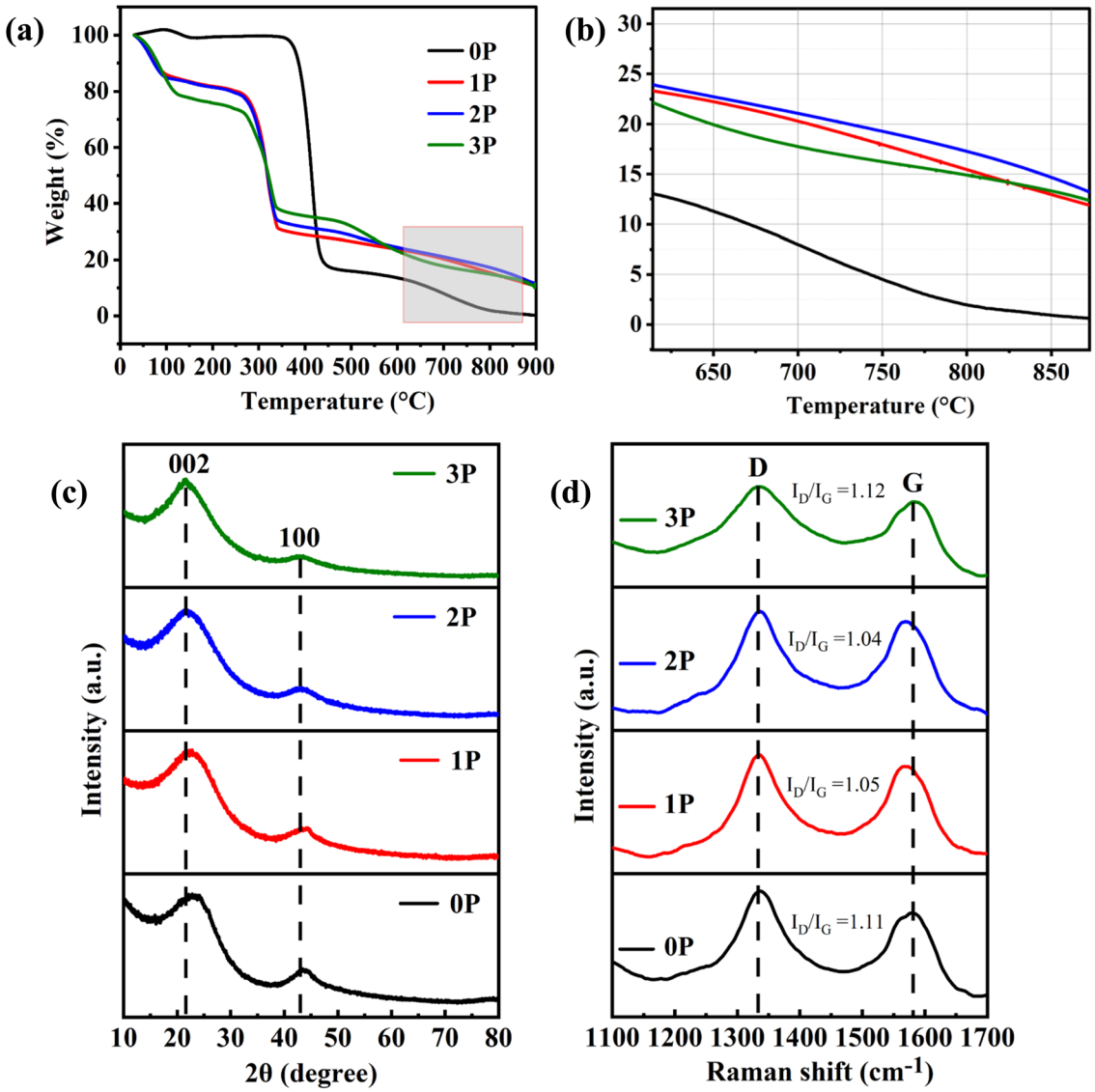

Fig. 3 Characterization results of PET-derived HC: (a) TGA curves of P-doped HC samples and undoped reference (0P); (b) zoomed TGA of a range 650–850 °C; (c) XRD patterns; (d) Raman spectra.

Table 1 Structural parameters of pristine and phosphorus-doped PET samples

Sample	$2\theta_{002}$	d_{002}[a] (nm)	L_c[a] (nm)	L_a[a] (nm)	L_c/d	I_D/I_G[b]
0P-HC	23.12	0.383	0.6237	1.2752	1.6286	1.11
1P-HC	22.40	0.397	0.6229	1.2736	1.5692	1.05
2P-HC	21.66	0.410	0.6222	1.2720	1.5175	1.04
3P-HC	21.42	0.415	0.6219	1.2715	1.4986	1.12

[a] Calculated and determined by XRD analysis. [b] Calculated and determined by Raman analysis.

(Horiba LabRam Evolution) with a 532 nm laser was used to probe the spectral region between 1100 and 1700 cm^{-1}. X-ray photoelectron spectroscopy (XPS) analysis was performed using a Thermo Scientific Nexsa XPS system, equipped with a monochromated Al Kα X-ray source (1486.6 eV), a 180° double-focusing hemispherical analyzer with a 128-channel detector, and a flood gun for charge compensation. High-resolution spectra were collected using adjustable spot sizes (10–400 μm) under standard instrument conditions. The specific surface area and pore size distribution of the samples were analyzed using nitrogen (N_2) adsorption on an ASAP 2020 V4.00C (V4.00C H) BET surface area and pore size analyzer.

The electrical properties of the samples, such as resistivity and conductivity, were obtained using the Hall effect measurement system (HMS-5500) at room temperature.

2.3. Electrochemical measurements

All electrochemical measurements were carried out at room temperature. The working electrode was prepared by mixing 80 wt% HC active materials, 10 wt% Super P (TIMCAL carbon black), and 10 wt% PVDF dissolved in NMP. The electrodes were

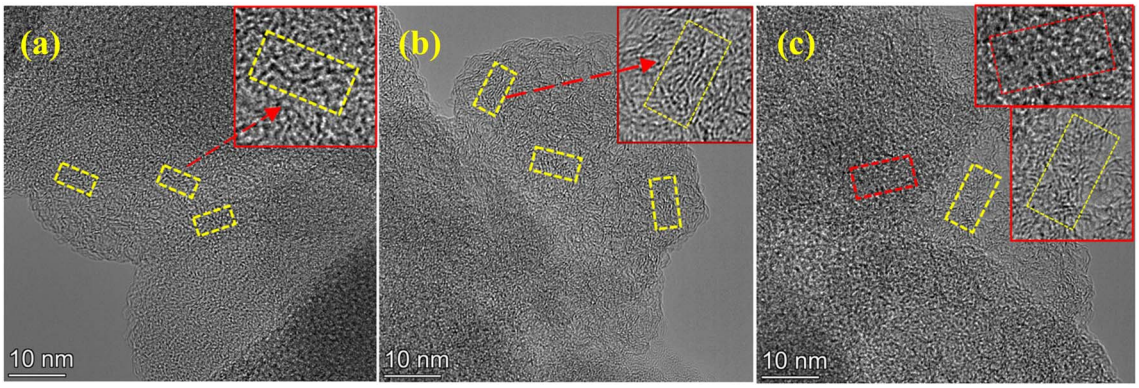

Fig. 4 High-resolution TEM images of (a) non-doped 0P and P-doped (b) 2P-HC, (c) 3P-HC samples. The yellow dashed lines in the images show graphene layers.

dried at 60 °C in a vacuum oven overnight to remove the solvent after coating the slurry on Cu foil. After the drying step, electrodes were calendered with a 10% thickness reduction using a roll-press machine. The electrodes were punched into 14 mm in diameter discs. Li metal was used as the counter/reference electrode, and Celgard 2400 polypropylene film as a separator. The electrolyte was a solution of 1 M $LiPF_6$ dissolved in a mixture of ethylene carbonate/dimethyl carbonate/diethyl carbonate (EC/DMC/DEC = 1 : 1 : 1 (v/v/v)) as solvents. To test

Table 2 Surface atomic composition (XPS, at%) and component ratios

Sample	C (at%)	O (at%)	P (at%)	P/C	P/O
HC-0P	87.01	12.99	—	—	—
HC-1P	83.91	13.74	2.35	0.0280	0.1710
HC-2P	80.91	16.12	2.97	0.0367	0.1842
HC-3P	81.36	15.14	3.50	0.0430	0.2311

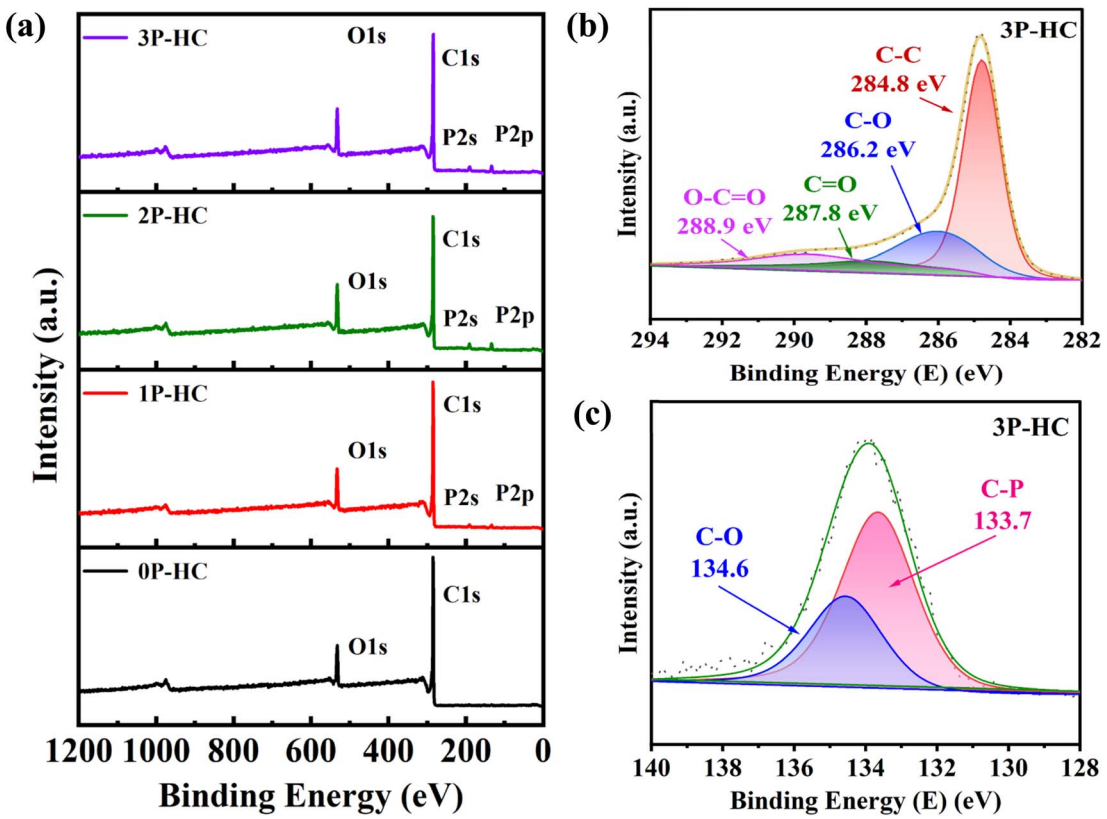

Fig. 5 XPS analysis of P-doped and undoped hard carbon samples: (a) XPS survey spectra of 0P-HC, 1P-HC, 2P-HC, and 3P-HC; (b) high-resolution C 1s spectrum and fit for 3P-HC; (c) high-resolution P 2p spectrum and fit for 3P-HC.

Table 3 Relative C 1s peak area ratios of 0P–3P samples

Sample	C–C	C–O	C=O	O–C=O	O-total	C–C/O-total
0P-HC	1	0.17	0.07	0.16	0.4	2.5
1P-HC	1	0.24	0.07	0.13	0.44	2.27
2P-HC	1	0.19	0.08	0.26	0.53	1.89
3P-HC	1	0.38	0.1	0.2	0.68	1.47

Table 4 The BET surface area results of HCs

Sample name	BET surface area, (m^2 g^{-1})	Total pore volume, (cm^3 g^{-1})
0P-HC	494.77	0.264
1P-HC	590.252	0.392
2P-HC	796.088	0.574
3P-HC	982.411	0.865
5P-HC	655.013	0.469

the electrochemical performance of the prepared electrodes in LIBs, the CR2032-type coin cells were assembled in an Ar-filled glovebox (MBRAUN, LABmaster Pro Glovebox, Germany, <0.1 ppm O_2 and <0.1 ppm H_2O). CV analysis was performed using a VMP3 potentiostat/galvanostat (Bio-Logic Science Instrument Co.) in a potential range of 0.01–3.0 V at a scan rate of 0.1 mV s^{-1}. The galvanostatic charge/discharge cycling was performed on a Neware battery tester between the cut-off voltages of 0.01–3.00 V *vs.* Li/Li^+ at a current density of 0.2 A g^{-1}. The rate capability cycling tests were performed between 0.01–3.00 V *vs.* Li/Li^+ at different current densities of 0.1 A g^{-1}, 0.2 A g^{-1}, 0.5 A g^{-1}, 1 A g^{-1}, 2 A g^{-1}. The specific capacities of all the half-cells were calculated based on the total mass of the HC, measured by ultramicrobalance (Mettler Toledo, XP6U). The mass loadings of the active materials were approximately 1.3–1.5 mg cm^{-2}. Electrochemical impedance spectroscopy (EIS) measurements were performed using a VMP3 potentiostat/galvanostat (Bio-Logic Science Instrument Co.) in the frequency range from 100 kHz to 10 mHz with an AC amplitude of 5 mV at open-circuit potential, after the 1st, 2nd, and 100th cycles.

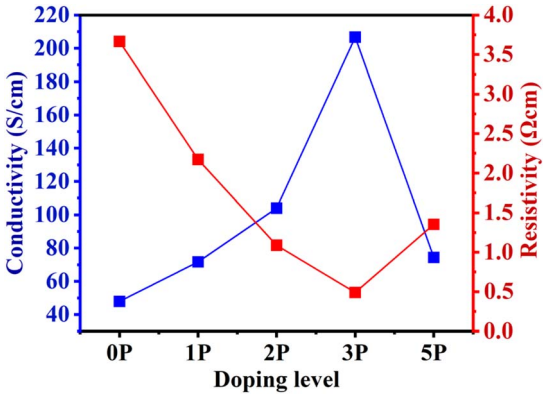

Fig. 7 Conductivity and resistivity results from Hall measurements for doped and non-doped electrodes.

3. Results and discussion

Following the synthesis, the morphological features of the obtained carbon materials were examined to reveal the effect of phosphorus doping on their structure. PET is a thermoplastic that melts during the carbonization process, resulting in pyrolysis products with a metallic luster.[22] The hard carbon samples carbonized without phosphorus doping generally exhibit a smooth and complete plate-like or blocky surface (Fig. 2a). In contrast, the P-doped HC samples show a more fragmented, porous, and rougher particle structure (Fig. 2b–e). Despite the increasing amounts of H_3PO_4 used, no significant visual differences were observed between the SEM images of the doped samples. This consistent appearance across samples suggests that while phosphorus doping influences the internal structural properties of the carbon matrix, it does not drastically alter the external morphology. The rougher and more porous nature of the P-doped HC samples may enhance ion accessibility and provide a higher surface area, potentially contributing to better electrochemical performance.

To further confirm the successful incorporation and spatial distribution of phosphorus within the carbon framework,

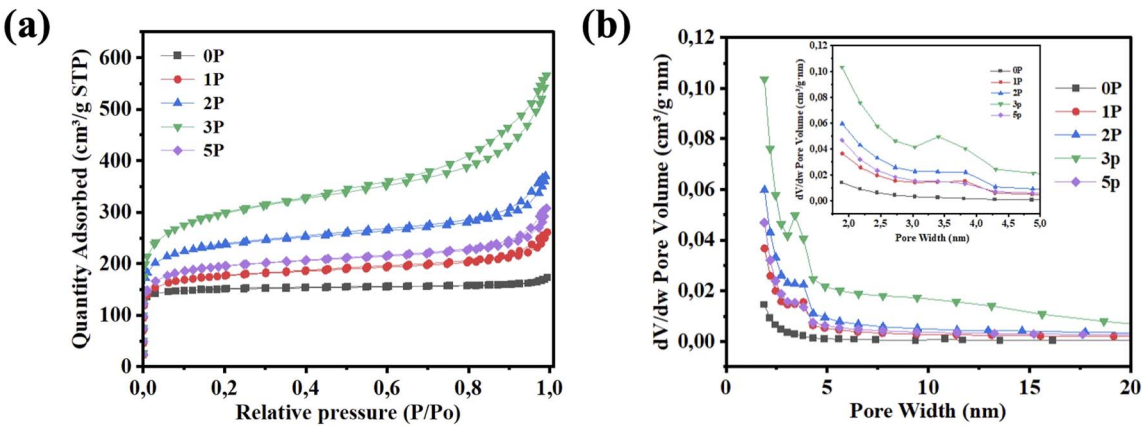

Fig. 6 (a) Nitrogen adsorption–desorption isotherms of phosphorus-doped HC samples; (b) PSD of phosphorus-doped HC samples.

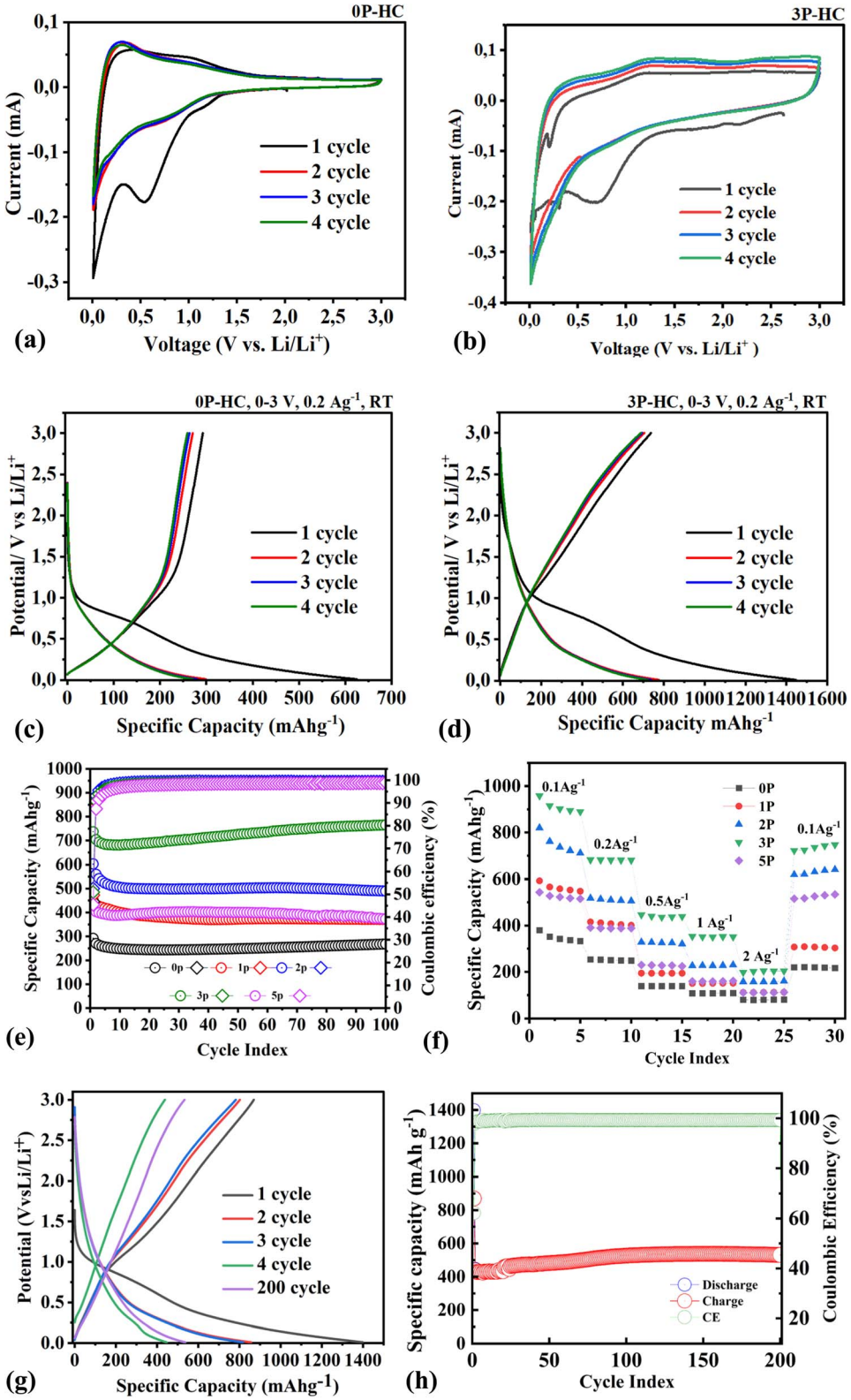

Fig. 8 Electrochemical performance of 0P-HC and 3P-HC anodes: (a and b) cyclic voltammetry (CV) curves at 0.1 mV s^{-1}; (c and d) galvanostatic charge–discharge profiles at 0.2 A g^{-1}; (e and f) cycling performance and rate capability; (g and h) long-term charge–discharge profiles and high-rate cycling at 0.5 A g^{-1} for 3P-HC.

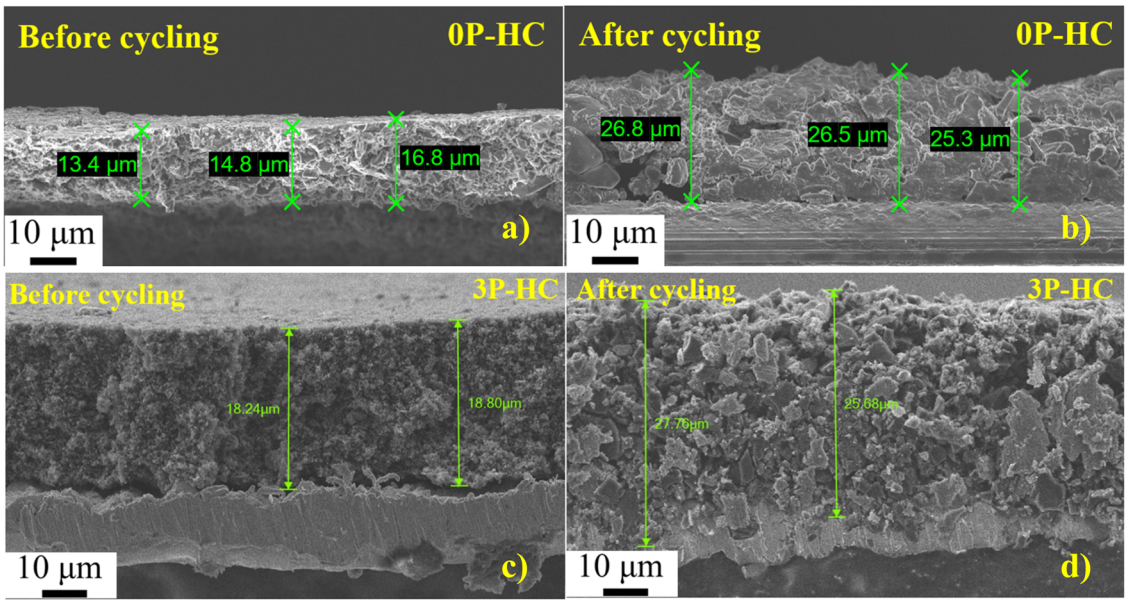

Fig. 9 SEM images of 0P and 3P electrodes before (a and c) and after (b and d) 100 cycles at 0.2 A g^{-1}.

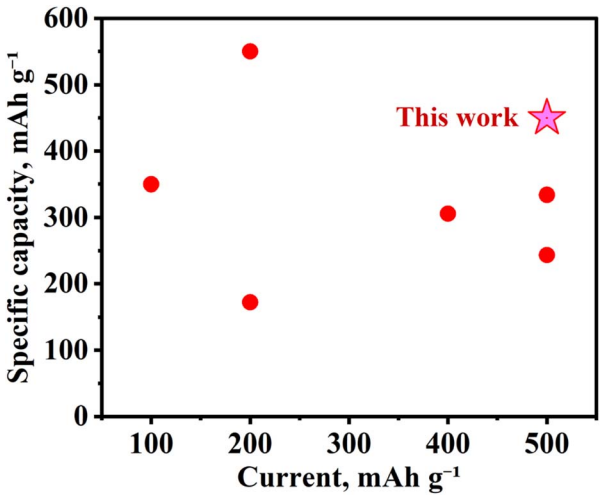

Fig. 10 Comparison of HCs for LIBs.

energy-dispersive X-ray spectroscopy (EDS) elemental mapping was performed (Fig. 2f–i). The EDS maps clearly show a uniform distribution of phosphorus alongside carbon and oxygen across the analyzed region, indicating that phosphorus atoms are homogeneously embedded within the carbon matrix rather than forming isolated clusters. This homogeneous dispersion of phosphorus suggests effective doping during the carbonization process and supports the structural modification inferred from the SEM observations.

Thermogravimetric analysis (TGA) was employed to evaluate the thermal stability, decomposition behavior, and carbon yield of pristine and P-PET samples, providing insight into the influence of P-doping on the carbonization process. Fig. 3a and b shows the TGA comparative results for the samples with and without doping. The TGA data of the pristine PET sample shows an initial weight loss beginning around 100 °C, attributed to the evaporation of residual solvents (TFA and DCM) and moisture. The thermal events between 400 °C and 600 °C reflect typical PET degradation processes, without the complex interactions seen in the case of P-PET. Residual weights at high temperatures are noted as 12.98% at 700 °C, 12.15% at 750 °C, and 11.36% at 800 °C, which are lower than those of P-HCs. The reduced yield is explained by the removal of benzene-containing functional groups.[38] During the carbonization process, part of the oxygen in 0P-PET converts into volatile compounds such as

Table 5 Comparison of the performance of the 3P-HC sample with other works' results

No.	Sample type	Carbon source	Current density, mA g^{-1}	Specific capacity, mAh g^{-1}	Reference
1	Biomass	Mangrove wood	500	334	51
2	Biomass	Sweet gum fruit	500	243.41	52
3	Waste derived	Unburned charcoal	100	350	53
4	Polymer	Waste PET	200	172	47
5	Biomass	Tannin	400	305.8	54
6	Porous PC	Lignin + $ZnCO_3$	200	550	55
7	**Polymer**	**Waste PET**	**500**	**531**	**This work**

CO_2 and H_2O, while the remaining oxygen contributes to the formation of cross-linked and turbostratic structures within the HC.

The higher residual weights of P-PET at higher temperatures compared to pristine PET suggest the formation of more thermally stable materials or additional char due to the chemical treatment. Complex thermal events between 400 °C and 600 °C are likely due to interactions between PET and the acids, leading to modified degradation pathways and new thermal degradation products with enhanced stability at higher temperatures.

To clarify the origin of the residual mass observed for the P-doped samples, an additional thermogravimetric analysis of the carbonized 3P-HC sample was performed in air (Fig. S3). The material is almost completely oxidized during heating, leaving only ~5.07 wt% residue at 800 °C. This remaining fraction can therefore be attributed to non-combustible phosphorus-containing inorganic species (phosphate-related ash), indicating that the obtained material consists predominantly of carbon (~95 wt%). These results demonstrate that the higher residual weight observed for the P-treated samples mainly reflects an increased carbon yield resulting from the H_3PO_4 treatment, rather than the accumulation of inorganic residues.

Diffraction analysis of the P-HC samples was performed in the range of 10° to 80° to observe the relative changes in the structure of the obtained HC materials. The XRD patterns (Fig. 3c) for the obtained samples display broad diffraction peaks around 2θ values of approximately 21° and 43°, which correspond to the typical planes in HC materials.

The broad peak around $2\theta \approx 21°$ is attributed to the (002) plane, which reflects the interlayer spacing in turbostratic carbon structures. The shift of the (002) peak towards a lower angle indicates a broader interlayer distance (d) as the concentration of the dopant increases. Accordingly, the d_{002} value observed from the XRD results for the 0P and 3P samples is 0.383 and 0.415 nm, respectively, which correlates with the TEM results. Besides, the broader diffraction peak pattern indicates smaller average crystallite sizes.[39] The layer spacing of the synthesized materials is calculated using the Bragg formula (eqn (1)) from the main diffraction peak (002):

$$d = \frac{\lambda}{2 \sin \theta} \quad (1)$$

where λ(0.15406 nm) represents the radiation wavelength, and θ is the angle of reflection. The thickness of crystallites (L_c) and the length of nanographitic domains (L_a) were measured using the following equation:

$$L = \frac{k\lambda}{\beta \cos \theta} \quad (2)$$

where β is the full width at half maximum (FWHM) of the diffraction peaks, and k is a constant, with values of 1.84 and 0.9 for the calculations of L_a and L_c, respectively.[40] The results are summarized in Table 1.

The Raman analysis of the carbonized samples doped with varying volumes of H_3PO_4 reveals two main peaks: the D-band centered around 1340 cm^{-1} and the G-band around 1590 cm^{-1} (Fig. 3d). The D peak is associated with defects and out-of-plane vibrations due to sp^3 bonding, while the G peak corresponds to the ordered graphitic structure with in-plane vibrations due to sp^2 aromatic bonding (C=C bonding).[41] The relative intensity ratios (I_D/I_G) were found to be 1.11 for 0P-HC, 1.05 for 1P-HC, 1.04 for 2P-HC, and 1.12 for 3P-HC, indicating an increase in defect density with higher doping levels.

The Raman spectra of the P-doped samples demonstrate an increase in the I_D/I_G ratio from 1.04 to 1.12 with increasing phosphorus content, reflecting a higher degree of structural disorder. Hard carbon materials with I_D/I_G values in the range of ~0.9–1.1 achieve an optimal balance between defect density, porosity, and cycling stability.[42] In this context, the observed ratios of 1.04–1.12 position the present samples within the optimal range, suggesting that the generated defects furnish abundant active sites for lithium storage while preserving sufficient electronic conductivity.

However, despite the beneficial increase in defect density up to 3P, further increases in doping, as seen in the 5P sample (Fig. S1), led to significant impurities due to corrosive reacting of orthophosphoric acid with the crucible during calcination, making the 4P and 5P samples unsuitable for optimal electrochemical performance. Thus, a balanced P-doping level is crucial for maintaining both the structural integrity and electrochemical activity of HC.

In the high-resolution TEM (HRTEM) image, the phosphorus-doped samples present a disordered amorphous structure in a large range, and part of the lattice stripes can be seen at the edges, indicating the existence of local order in the disordered structure (Fig. 4). Compared to non-doped carbon, which has an interlayer distance of 0.375 nm, the phosphorus-doped 3P-HC sample exhibits a larger interlayer spacing of approximately 0.411 nm. This increased interlayer distance facilitates the transport and storage of Li-ions, thereby enhancing the electrochemical performance of the anode material.

The surface composition and bonding environments of pristine and P-HC samples were examined by XPS. The full survey spectra in Fig. 5a display prominent C 1s and O 1s peaks for all samples. In contrast, distinct P 2s and P 2p peaks appear only in the doped samples (1P–3P), confirming the successful incorporation of phosphorus into the carbon framework.

The quantitative surface compositions are summarized in Table 2. The pristine 0P-HC sample consists of 87.01 at% C and 12.99 at% O. Upon phosphorus doping, the P content gradually increases from 2.35 at% in 1P-HC to 3.50 at% in 3P-HC. Correspondingly, the P/C and P/O ratios increase steadily from 0.0280 and 0.1710 in 1P-HC to 0.0430 and 0.2311 in 3P-HC, respectively. This trend demonstrates that phosphorus is incorporated in a controlled manner, with higher acid content leading to progressively higher surface phosphorus concentrations, consistent with previous reports where increasing phosphorus-source content resulted in simultaneous enrichment of surface P and O species in hard carbon materials.[43] At the same time, the relative C content decreases, reflecting the replacement or modification of carbon sites by phosphorus- and oxygen-containing functional groups.

The high-resolution C 1s spectra (Fig. 5b) provide further insight into the bonding evolution. The spectra can be deconvoluted into four components: C–C/C=C at 284.8 eV, C–O at 286.2 eV, C=O at 287.8 eV, and O–C=O at 288.9 eV.[44] The relative peak area ratios are summarized in Table 3. In the pristine 0P-HC sample, the C–C component dominates, and the overall oxygenated species (O-total) are relatively low (0.40, normalized to C–C = 1). As phosphorus doping increases, the fraction of oxygenated carbon progressively rises: O-total increases from 0.44 in 1P-HC to 0.68 in 3P-HC. Concomitantly, the C–C/O-total ratio decreases from 2.50 (0P-HC) to 1.47 (3P-HC) (Fig. S2). This clear shift indicates that phosphorus doping induces oxidation of the carbon surface and introduces abundant functional groups such as C–O and O–C=O. These changes increase defect density and surface polarity, which are beneficial for electrolyte wettability and provide additional active sites for lithium storage.

The P 2p spectrum of the 3P-HC sample (Fig. 5c) further confirms the bonding states of phosphorus. Two peaks are observed at 133.7 eV and 134.6 eV, corresponding to P–C and P–O bonds, respectively.[44,45] The presence of P–C indicates covalent bonding between phosphorus and the carbon lattice, which enhances electronic conductivity by introducing electron-deficient sites. Meanwhile, P–O species correspond to phosphate-related groups on the surface, which may stabilize the structure during cycling.

Porosity plays a crucial role in determining the electrochemical performance of hard carbon anodes, as it governs ion transport pathways and the accessibility of active sites. To further elucidate the porous structure and surface characteristics of the P-HC samples, N_2 adsorption–desorption measurements were conducted. The BET surface area and pore volume data for the non-doped and P-HC samples are summarized in Table 4, revealing a clear dependence of textural properties on phosphorus content. Among these, the 3P-HC sample exhibits the highest BET surface area (982.41 $m^2\ g^{-1}$) and total pore volume (0.8646 $cm^3\ g^{-1}$), suggesting that an intermediate phosphorus doping level promotes the formation of a well-developed porous framework. Such enhanced porosity is essential for efficient lithium-ion storage, providing abundant active sites and facilitating electrolyte infiltration and ion diffusion within the carbon matrix.

In comparison, the undoped 0P-HC and lightly doped 1P-HC samples show considerably lower surface areas (494.77 and 590.25 $m^2\ g^{-1}$, respectively), indicating less accessible pore structures. These findings demonstrate that moderate phosphorus incorporation effectively optimizes the balance between structural integrity and porosity, leading to a hierarchical network favorable for electrochemical performance.

According to Fig. 6, the BET (Brunauer–Emmett–Teller) analysis reveals that the isotherms for the samples 0P–5P exhibit a combined microporous–mesoporous character (Type I/IV). The sharp uptake at low relative pressures ($P/P_0 < 0.1$) is characteristic of micropore filling, while the hysteresis loop observed at intermediate relative pressures ($0.4 < P/P_0 < 0.9$) is indicative of capillary condensation in mesopores, consistent with Type IV behavior.[46] The steep rise at high relative pressures ($P/P_0 > 0.8$) further suggests the presence of larger mesopores or macropores, confirming a hierarchical pore structure.

The pore size distribution (PSD) analysis further supports these observations. The PSD plot shows a predominant peak in pore widths around 2–4 nm for all samples, confirming the presence of mesopores as the dominant pore type. The micropore contribution, evidenced by the low-pressure uptake in the isotherms, complements the mesoporous framework. Additionally, the quantity adsorbed significantly decreases for pore widths above 10 nm, indicating a lower prevalence of macropores. Notably, the 3P sample exhibits a higher overall quantity adsorbed compared to the 5P sample, suggesting that the 3P sample has a higher porosity or more available adsorption sites.

The impact of P-doping on the electronic properties of the P-HC electrodes was examined through Hall effect measurements, with the results displayed in Fig. 7. Among the samples, 3P-HC demonstrated the lowest resistivity and highest mobility, achieving a peak conductivity of 206.69 S cm^{-1} (as shown in Table S1).

The increase in conductivity with rising P content suggests that P atoms integrate into the carbon lattice, generating electron-deficient sites (holes) which boost carrier mobility and conductivity within the material.[25]

The CV measurements were conducted to analyze the lithiation and delithiation processes, identify the formation of the solid electrolyte interphase (SEI) layer, and assess the stability of the P-HC anodes over multiple cycles. Fig. 8a and b show the CV curves which were performed at a scan rate of 0.1 mV s^{-1} between the cut-off voltages of 0.01 and 3.0 V (*vs.* Li/Li^+) at 25 °C. Observed during the negative-going scan, reduction peaks indicate the intercalation of lithium ions into the P-HC anode. The initial reduction peak around 0.7 V in the first cycle suggests the formation of the SEI layer, which stabilizes in subsequent cycles. During the positive-going scan, oxidation (delithiation) peaks represent the deintercalation of lithium ions from the P-HC anode. The oxidation peaks around 1.2 V to 2.1 V in the first cycle get more intense in later cycles, indicating a more stable and consistent electrochemical behavior. Also, the increased peak height and area observed in the CV analysis of the P-doped anode materials indicate superior electrochemical performance compared to the non-doped anode.[46]

According to the widely accepted model of the lithiation mechanism in HC, the process proceeds through two main voltage regions:[47] a sloping region at higher potentials (approximately 0.1–3.0 V *vs.* Li/Li^+), dominated by surface adsorption onto defect sites and intercalation into disordered/turbostratic carbon domains; and a plateau region at near-zero potentials ($<\sim$0.1 V *vs.* Li/Li^+), associated with quasi-metallic lithium filling of closed nanopores. P-doping markedly increases the porosity, surface area, and structural disorder of the carbon matrix, thereby expanding both the slope capacity—through additional adsorption sites and defect-mediated intercalation—and the plateau capacity, by promoting the formation of closed nanopores. The enlarged interlayer spacing in the turbostratic domains of P-doped samples, as corroborated by XRD and HRTEM results, further facilitates lithium intercalation within the sloping region.

Overall, the substantial improvement in specific capacity can be ascribed not only to the enhanced structural properties on the surface and within the anode material but also to an increase in the material's electrical conductivity, imparted by the phosphorus doping.[48]

Fig. 8c and d present the galvanostatic charge–discharge (GCD) curves for the 0P and 3P samples during the initial four cycles at a relatively high current density of 0.2 A g^{-1}. The 3P sample (HC-3P) shows a relatively flat discharge profile approximately below 0.2 V, which corresponds to the nanopore-filling of lithium ions within the anode structure. In contrast, the GCD curves for the 0P sample display a sloping profile across a potential range of 0.01–3 V, suggesting that the capacity in this sample is primarily influenced by surface-induced capacitive processes.[18]

To further clarify the lithiation/delithiation mechanisms and exclude possible parasitic reactions responsible for the gradual capacity increase, differential capacity (dQ/dV) analysis was performed based on the galvanostatic charge–discharge profiles. The corresponding dQ/dV curves for the 0P-HC and 3P-HC electrodes at selected cycles are presented in Fig. S4a and b.

For the 0P-HC electrode (Fig. S4a), the first cathodic scan exhibits a broad reduction feature extending from ~1.0 to ~0.2 V, with a maximum around ~0.6–0.7 V. This broad signal is associated with electrolyte decomposition and the formation of the SEI on the fresh carbon surface. In addition, a steep feature observed below ~0.1 V corresponds to lithium insertion into the disordered carbon structure and filling of nanopores, which is characteristic of hard carbon materials. After the first cycle, the high-potential reduction feature becomes significantly weaker, indicating that the majority of SEI formation occurs during the initial lithiation. In subsequent cycles, the dQ/dV curves become smoother and largely overlap, suggesting stabilization of the electrode/electrolyte interface and the establishment of reversible lithium storage processes.

The 3P-HC electrode (Fig. S4b) exhibits similar electrochemical features but with several notable differences. The cathodic response below ~0.1 V becomes more pronounced and better defined, indicating enhanced lithium storage in nanopores and defect sites created by phosphorus doping. Meanwhile, the broad irreversible feature related to SEI formation in the first cycle is slightly less pronounced compared with the undoped sample, suggesting modified surface chemistry and improved interfacial stability.

Importantly, during prolonged cycling, the positions of the cathodic and anodic features remain stable, while their intensity gradually increases and the curves progressively overlap from the 10th to the 100th cycle. No sharp and isolated peaks appear in the near-zero potential region during lithiation or delithiation, which are typically associated with lithium plating/stripping processes. Instead, the smooth evolution of the dQ/dV profiles indicates that the gradual capacity increase observed during cycling originates from progressive electrochemical activation of the porous carbon framework rather than metallic lithium deposition.

This activation behavior can be attributed to improved electrolyte penetration into the hierarchical pore structure and gradual utilization of additional lithium storage sites introduced by phosphorus-induced defects and expanded interlayer spacing.

In Fig. 8e, the cycling performances of non-doped and P-HC electrodes are shown at a current density of 0.2 A g^{-1} over 100 cycles. The 3P-HC anode material demonstrates a high initial specific capacity (~737 mAh g^{-1}) and stable performance throughout the cycling test, with the first cycle influenced by the formation of an SEI layer, impacting the initial capacity. As expected for HC-based anodes, all samples exhibit a gradual decrease in specific capacity during the initial cycles while showing an increase in CE, which is typical behavior due to the low initial coulombic efficiency (ICE) often seen in HC anodes.

The ICE values calculated from the first charge–discharge cycle at 0.2 A g^{-1} are 46.8%, 49.6%, 52.5%, 50.9%, and 45.4% for 0P-HC, 1P-HC, 2P-HC, 3P-HC, and 5P-HC, respectively. The relatively low ICE is mainly attributed to irreversible lithium consumption associated with SEI formation and reactions with abundant oxygen-containing surface groups and defects in PET-derived hard carbon. Moderate phosphorus incorporation slightly improves the ICE compared with the undoped sample, with the highest value observed for 2P-HC, suggesting that phosphorus-induced modification of the carbon surface chemistry partially stabilizes the electrode–electrolyte interface. The relatively low ICE values observed across all samples are consistent with the known challenges of high-surface-area, oxygen-rich hard carbon precursors and could be addressed through the electrolyte optimization, pre-lithiation, and surface-engineering strategies.

A notable observation is that all samples up to 3P-HC demonstrate an increase in capacity after several cycles. This phenomenon is likely due to the activation process within the HC material and phosphorus-based activation reactions, which gradually enhance lithium-ion storage. This incremental capacity improvement is consistent with previous research, suggesting that P-doping introduces additional electrochemical activation pathways in the carbon matrix, potentially unlocking more storage sites and improving conductivity with extended cycling.[22] The similar trends in specific capacity increase and decrease observed in both 3P and 0P samples further support the hypothesis that P-doping amplifies the activation of HC, thereby enhancing its overall electrochemical performance.

The rate capability of P-HC anodes was evaluated at various current densities ranging from 0.1 A g^{-1} to 2 A g^{-1} (Fig. 8f). As a comparison, the same test was conducted on the non-doped 0P sample. At a low current density of 0.1 A g^{-1}, all P-HC samples exhibited higher initial specific capacities compared to the non-doped sample, which remained stable over 25 cycles, demonstrating excellent capacity retention and stability. Overall, the correlation between rate capability and cycling performance aligns, indicating the P-doped samples' ability—particularly the 3P sample—to maintain stable and robust performance across a range of current densities. The remarkable electrochemical performance of 3P can be attributed to its distinctive microstructure, featuring an increased density of graphitic nanodomains and appropriately sized nanovoids, which likely serve as additional active sites for Li^+ ion storage.

At a high current density of 0.5 A g^{-1}, the 3P-HC electrode exhibits outstanding cycling stability and rate capability (Fig. 8f and h). The galvanostatic charge–discharge profiles retain a distinct plateau below 0.2 V, characteristic of lithium insertion into nanopores, and display nearly identical shapes even after 200 cycles, evidencing excellent structural reversibility and low polarization growth. The corresponding cycling performance reveals a gradual increase in specific capacity during the initial 120 cycles. Following this stage, the electrode delivers a highly stable reversible capacity over prolonged cycling, underscoring the robust electrochemical kinetics and durable architecture imparted by phosphorus doping.

Electrochemical impedance spectroscopy (EIS) was conducted to further investigate the interfacial kinetics and charge-transfer evolution of the 0P-HC and 3P-HC electrodes. The Nyquist plots collected after the 1st, 2nd, and 100th cycles are presented in Fig. S5. In both electrodes, the impedance spectra display three characteristic regions: a high-frequency intercept corresponding to the electrolyte and contact resistance (R_s), a depressed semicircle in the high- to mid-frequency region associated with the combined surface film and charge-transfer resistance (R_{SEI} + R_{ct}), and an inclined low-frequency region related to Li^+ diffusion within the carbon framework.

For the undoped 0P-HC electrode, R_s decreases from 52.6 Ω (1st cycle) to 41.3 Ω (100th cycle)—a ∼21% reduction attributable to progressive electrolyte infiltration into the accessible pore network, which lowers the overall ohmic resistance of the electrode–electrolyte system. This wetting effect, however, does not translate into improved charge-transfer kinetics: the R_{ct}, estimated from the low-frequency end of the depressed semicircle, increases from approximately 165 Ω to 200 Ω—also a 21% rise—over the same cycling period. The $-Z''$(max) of the semicircle decreases marginally from 60.6 Ω to 52.5 Ω, indicating a geometric change in the interfacial layer rather than a reduction in its resistance. This divergence between decreasing R_s and increasing R_{ct} reflects two competing processes: electrolyte penetration progressively wets the high-surface-area carbon (reducing bulk ohmic losses), while concurrent SEI growth at the carbon–electrolyte interface impedes faradaic charge transfer. The net result is deteriorating interfacial kinetics in the undoped electrode, as further evidenced by the progressively extended low-frequency diffusion tail.

The 3P-HC electrode exhibits markedly different impedance behavior. The R_s values of 10.8 Ω, 12.0 Ω, and 15.6 Ω after the 1st, 2nd, and 100th cycles, respectively, are approximately 3–5 times lower than those of 0P-HC, consistent with the substantially improved electronic conductivity of the phosphorus-doped carbon framework confirmed by Hall effect measurements (206.69 S cm^{-1}). More importantly, the R_{ct} of 3P-HC decreases systematically from approximately 122 Ω after the 1st cycle to 83 Ω after the 2nd cycle and 66 Ω after the 100th cycle—a total reduction of 46%. This progressive decrease directly confirms the gradual electrochemical activation of the P-doped carbon framework during cycling, consistent with the capacity increase observed in long-term galvanostatic measurements (Fig. 8e). After 100 cycles, R_{ct} of 3P-HC (66 Ω) is approximately 3.0 times lower than that of 0P-HC (200 Ω), demonstrating a substantial kinetic advantage conferred by phosphorus incorporation.

In the low-frequency region, the impedance response of 3P-HC displays a distinctly curved diffusion tail rather than the linear Warburg behavior observed for 0P-HC. Such behavior is characteristic of finite-length Li^+ diffusion through a hierarchical pore network, where ions traverse pathways of distributed lengths and geometries, leading to deviation from the ideal semi-infinite Warburg response.[49,50] This observation is consistent with the well-developed hierarchical pore structure of 3P-HC, as evidenced by the Type I/IV N_2 adsorption isotherms and high total pore volume (0.865 cm^3 g^{-1}), and confirms that the hierarchical porosity introduced by phosphorus doping facilitates distributed but efficient Li^+ transport pathways within the electrode.

Furthermore, the cells were disassembled, and SEM analysis was conducted to assess the state of the 0P and 3P electrodes after 100 cycles at 0.2 A g^{-1}. Fig. 9a and c show the electrode morphology before cycling, while Fig. 9b and d illustrate it after cycling. The cross-sectional images reveal an increase in thickness after cycling, along with particle agglomeration. Despite these changes, good adhesion and integrity between the current collector and the active material are maintained, indicating the stability and resilience of the electrode materials even after prolonged cycling.

In summary, the P-doped HC samples, particularly 3P, demonstrated remarkable rate capability and stability across a range of current densities. Their ability to maintain high specific capacities and recover after high-rate cycling positions them as superior materials for applications requiring robust electrochemical performance.

To highlight the benefits of the obtained results, Fig. 10 provides a summary of the specific capacities of anode materials from different HCs obtained at different current densities (the results are summarized in Table 5). These findings, along with the comparison presented, indicate that synthesizing plastic-derived HC from PET bottles as an anode material shows an advantage. The stable specific capacity of 3P-HC 531 mAh g^{-1} at 500 mA g^{-1} underscores its excellent performance as an anode material for LIBs.

4. Conclusion

This study investigated the preparation of phosphorus-doped hard carbon derived from PET through a single-step carbonization process using orthophosphoric acid. TGA analysis indicated enhanced thermal stability and higher carbon yield for the phosphorus-doped samples compared to the untreated ones. The introduction of H_3PO_4 significantly enhances char formation and thermal stability, as evidenced by higher residual weights and complex degradation pathways. In contrast, 0P, treated with TFA-DCM without H_3PO_4, exhibits typical PET degradation behavior with lower residual weights, indicating less thermal stability.

Phosphorus doping significantly altered the carbon structure, as evidenced by X-ray diffraction (XRD) analysis, which showed increased interlayer spacing (d_{002} from 0.383 nm for 0P-

HC to 0.415 nm for 3P-HC) and higher structural disorder (I_D/I_G from 1.04 to 1.12), resulting in more amorphous carbon characteristics with abundant active sites for lithium storage. The broadened XRD peaks indicated the presence of turbostratic carbon structures.

Nitrogen adsorption–desorption isotherms demonstrated that the P-HC samples exhibited Type I/IV isotherms, indicative of a hierarchical microporous–mesoporous structure. The BET analysis confirmed a high surface area of 982.41 $m^2\ g^{-1}$ and a total pore volume of 0.865 $cm^3\ g^{-1}$ for 3P-HC, with the combined isotherm character indicating a hierarchical pore network that facilitates electrolyte infiltration and ion transport.

Electrochemical evaluation revealed that the P-HC anodes, particularly 3P-HC, exhibited superior performance with high specific capacities and excellent rate capabilities. The reversible capacity of 3P-HC reached 765 mAh g^{-1} after 100 cycles at 0.2 A g^{-1}, representing an increase from the initial value of ~737 mAh g^{-1}, significantly outperforming non-doped PET-derived carbon. The initial coulombic efficiency of 3P-HC is 50.9%, owing to its higher surface area and greater density of defect sites, and represents a known limitation of high-surface-area, oxygen-rich hard carbon precursors addressable through electrolyte optimization or pre-lithiation. Differential capacity analysis confirmed that the gradual capacity increase during cycling originates from progressive electrochemical activation of the porous carbon framework rather than lithium plating. Electrochemical impedance spectroscopy further demonstrated that phosphorus doping reduces the charge-transfer resistance from ~165 Ω (0P-HC) to ~66 Ω (3P-HC) after 100 cycles, and drives a 46% decrease in R_{ct} over prolonged cycling, consistent with the activation behavior observed in galvanostatic measurements.

Conflicts of interest

The authors declare no conflict of interest.

Data availability

The data supporting the findings of this study are available in the supplementary information (SI) of this article. Supplementary information is available. See DOI: https://doi.org/10.1039/d6ta00836d.

Acknowledgements

This research was funded by the Research Targeted Programs" BR24992766 "Development of methods and technologies for environmentally friendly "green" processing of polymer waste for energy storage" from the Ministry of Science and Higher Education of the Republic of Kazakhstan.

References

1 X. Chen, Y. Wang and L. Zhang, Recent Progress in the Chemical Upcycling of Plastic Wastes, *ChemSusChem*, 2021, **14**, 4137–4151, DOI: 10.1002/cssc.202100868.
2 B. Hu, S. Wang, J. Yan, H. Zhang, L. Qiu, W. Liu, Y. Guo, J. Shen, B. Chen, C. Shi and X. Ge, Review of waste plastics treatment and utilization: Efficient conversion and high value utilization, *Process Saf. Environ. Prot.*, 2024, **183**, 378–398, DOI: 10.1016/j.psep.2024.01.024.
3 J. Chen, J. Wu, P. C. Sherrell, J. Chen, H. Wang, W. Zhang and J. Yang, How to Build a Microplastics-Free Environment: Strategies for Microplastics Degradation and Plastics Recycling, *Advanced Science*, 2022, **9**, 2103764, DOI: 10.1002/advs.202103764.
4 K. Zhang, A. H. Hamidian, A. Tubić, Y. Zhang, J. K. H. Fang, C. Wu and P. K. S. Lam, Understanding plastic degradation and microplastic formation in the environment: A review, *Environ. Pollut.*, 2021, **274**, 116554, DOI: 10.1016/j.envpol.2021.116554.
5 O. García-Depraect, S. Bordel, R. Lebrero, F. Santos-Beneit, R. A. Börner, T. Börner and R. Muñoz, Inspired by nature: Microbial production, degradation and valorization of biodegradable bioplastics for life-cycle-engineered products, *Biotechnol. Adv.*, 2021, **53**, 107772, DOI: 10.1016/j.biotechadv.2021.107772.
6 X. Zhao and F. You, Life Cycle Assessment of Microplastics Reveals Their Greater Environmental Hazards than Mismanaged Polymer Waste Losses, *Environ. Sci. Technol.*, 2022, **56**, 11780–11797, DOI: 10.1021/acs.est.2c01549.
7 D. Chen, K. Luo, Z. Yang, Y. Zhong, Z. Wu, Y. Song, G. Chen, G. Wang, B. Zhong and X. Guo, Direct conversion of ester bond-rich waste plastics into hard carbon for high-performance sodium storage, *Carbon*, 2021, **173**, 253–261, DOI: 10.1016/j.carbon.2020.11.004.
8 M. R. Santos, L. C. Dias, M. C. Cunha and J. R. Marques, Multicriteria Decision Analysis Addressing Marine and Terrestrial Plastic Waste Management: A Review, *Front. Mar. Sci.*, 2022, **8**, 747712, DOI: 10.3389/fmars.2021.747712.
9 J. Su, T. Li, W. Xie, C. Wang, L. Yin, T. Yan and K. Wang, Emerging Technologies for Waste Plastic Treatment, *ACS Sustainable Chem. Eng.*, 2023, **11**, 8176–8192, DOI: 10.1021/acssuschemeng.2c07462.
10 D. Damayanti, D. R. Saputri, D. S. S. Marpaung, F. Yusupandi, A. Sanjaya, Y. M. Simbolon, W. Asmarani, M. Ulfa and H.-S. Wu, Current Prospects for Plastic Waste Treatment, *Polymers*, 2022, **14**, 3133, DOI: 10.3390/polym14153133.
11 M. S. S. R. Tejaswini, P. Pathak, S. Ramkrishna and P. S. Ganesh, A comprehensive review on integrative approach for sustainable management of plastic waste and its associated externalities, *Sci. Total Environ.*, 2022, **825**, 153973, DOI: 10.1016/j.scitotenv.2022.153973.
12 R. Wei, G. von Haugwitz, L. Pfaff, J. Mican, C. P. S. Badenhorst, W. Liu, G. Weber, H. P. Austin, D. Bednar, J. Damborsky and U. T. Bornscheuer, Mechanism-Based Design of Efficient PET Hydrolases, *ACS Catal.*, 2022, **12**, 3382–3396, DOI: 10.1021/acscatal.1c05856.
13 P. Benyathiar, P. Kumar, G. Carpenter, J. Brace and D. K. Mishra, Polyethylene Terephthalate (PET) Bottle-to-Bottle Recycling for the Beverage Industry: A Review, *Polymers*, 2022, **14**, 2366, DOI: 10.3390/polym14122366.

14 Y. Ding, Z. P. Cano, A. Yu, J. Lu and Z. Chen, Automotive Li-Ion Batteries: Current Status and Future Perspectives, *Electrochem. Energy Rev.*, 2019, **2**, 1–28, DOI: 10.1007/s41918-018-0022-z.

15 X. Lu, J. Zhou, X. Li, H. Peng, C. Shi, F. Liu, L. Huang and Z. Sun, In Situ Composite Strategy of O/F-Dual-Doped Soft–Hard Carbon Anode Promotes Ultrafast and Highly Durable Potassium Storage Performance, *ACS Appl. Mater. Interfaces*, 2025, **17**, 29708–29719, DOI: 10.1021/acsami.5c04171.

16 M. Jiang, X. Wang, W. Xi, H. Zhou, P. Yang, J. Yao, X. Jiang and D. Wu, Upcycling plastic waste to carbon materials for electrochemical energy storage and conversion, *Chem. Eng. J.*, 2023, **461**, 141962, DOI: 10.1016/j.cej.2023.141962.

17 A. Mirjalili, Towards Upcycling Polyethylene Terephthalate (PET) Plastic Waste for Energy Storage, *PhD thesis*, University of California, Riverside, 2021, https://www.proquest.com/docview/2565163334/abstract/4E45124501E049B9PQ/1.

18 C. O. Ehi-Eromosele, C. N. Onwucha, S. O. Ajayi, G. Melinte, A.-L. Hansen, S. Indris and H. Ehrenberg, Ionothermal synthesis of activated carbon from waste PET bottles as anode materials for lithium-ion batteries, *RSC Adv.*, 2022, **12**, 34670–34684, DOI: 10.1039/D2RA06786B.

19 S. Wu, H. Peng, L. Huang, Y. Liu, Y. Wu, L. Liu, W. Ai and Z. Sun, P-doped hard carbon microspheres for sodium-ion battery anodes with superior rate and cyclic performance, *Inorg. Chem. Front.*, 2023, **10**, 5908–5916, DOI: 10.1039/D3QI01296D.

20 H. Tao, S. Du, F. Zhang, L. Xiong, Y. Zhang, H. Ma and X. Yang, Achieving a High-Performance Carbon Anode through the P–O Bond for Lithium-Ion Batteries, *ACS Appl. Mater. Interfaces*, 2018, **10**, 34245–34253, DOI: 10.1021/acsami.8b11243.

21 H. Zhu, D. Wu, G. Zhang, W. Xu, A. Wang and K. Sun, The effects of doped phosphorus on the electrochemical performance of hard carbon anode for lithium ion capacitors, *J. Energy Storage*, 2023, **57**, 106172, DOI: 10.1016/j.est.2022.106172.

22 S. Alvin, C. Chandra and J. Kim, Extended plateau capacity of phosphorus-doped hard carbon used as an anode in Na- and K-ion batteries, *Chem. Eng. J.*, 2020, **391**, 123576, DOI: 10.1016/j.cej.2019.123576.

23 L. Deng, Y. Tang, J. Liu, Y. Zhang, W. Song, Y. Li and L. Liu, Phosphate-Induced Reaction to Prepare Coal-Based P-Doped Hard Carbon with a Hierarchical Porous Structure for Improved Sodium-Ion Storage, *Molecules*, 2023, **28**, 4921, DOI: 10.3390/molecules28134921.

24 F. Wu, R. Dong, Y. Bai, Y. Li, G. Chen, Z. Wang and C. Wu, Phosphorus-Doped Hard Carbon Nanofibers Prepared by Electrospinning as an Anode in Sodium-Ion Batteries, *ACS Appl. Mater. Interfaces*, 2018, **10**, 21335–21342, DOI: 10.1021/acsami.8b05618.

25 X. Wang, M. Hou, Z. Shi, X. Liu, I. Mizota, H. Lou, B. Wang and X. Hou, Regulate Phosphorus Configuration in High P-Doped Hard Carbon as a Superanode for Sodium Storage, *ACS Appl. Mater. Interfaces*, 2021, **13**, 12059–12068, DOI: 10.1021/acsami.0c23165.

26 S. Wu, H. Peng, J. Xu, L. Huang, Y. Liu, X. Xu, Y. Wu and Z. Sun, Nitrogen/phosphorus co-doped ultramicropores hard carbon spheres for rapid sodium storage, *Carbon*, 2024, **218**, 118756, DOI: 10.1016/j.carbon.2023.118756.

27 C. Lin, G. Suo, R. Mu, B. Zhao, J. Li, X. Hou, X. Ye, Y. Yang and L. Zhang, Dual carbon confining SnO2 nanocrystals as high-performance anode for sodium-ion batteries, *J. Power Sources*, 2024, **623**, 235426, DOI: 10.1016/j.jpowsour.2024.235426.

28 G. Suo, B. Zhao, R. Mu, C. Lin, S. Javed, X. Hou, X. Ye, Y. Yang and L. Zhang, Dual carbon confined MoS2 hierarchical microspheres as high-performance anode for sodium-ion batteries with superior cycling stability, *J. Energy Storage*, 2024, **77**, 109801, DOI: 10.1016/j.est.2023.109801.

29 B. Zhao, G. Suo, R. Mu, C. Lin, J. Li, X. Hou, X. Ye, Y. Yang and L. Zhang, Constructing hierarchical MoS2/WS2 heterostructures in dual carbon layer for enhanced sodium ions batteries performance, *J. Colloid Interface Sci.*, 2024, **668**, 565–574, DOI: 10.1016/j.jcis.2024.04.194.

30 H. Hou, L. Shao, Y. Zhang, G. Zou, J. Chen and X. Ji, Large-Area Carbon Nanosheets Doped with Phosphorus: A High-Performance Anode Material for Sodium-Ion Batteries, *Advanced Science*, 2017, **4**, 1600243, DOI: 10.1002/advs.201600243.

31 N. Li, Q. Yang, Y. Wei, R. Rao, Y. Wang, M. Sha, X. Ma, L. Wang and Y. Qian, Phosphorus-doped hard carbon with controlled active groups and microstructure for high-performance sodium-ion batteries, *J. Mater. Chem. A*, 2020, **8**, 20486–20492, DOI: 10.1039/D0TA06910H.

32 Y. Liu, J. Sun, S. Zhang, H. Zhang, P. Wang, J. Guo and S. Geng, Research Progress on Phosphorus/Carbon Anode Materials for Sodium-Ion Batteries, *ACS Omega*, 2025, **10**, 32511–32531, DOI: 10.1021/acsomega.5c00672.

33 X. Lan, Z. Li, Y. Zeng, C. Han, J. Peng and H.-M. Cheng, Phosphorus-based anodes for fast-charging alkali metal ion batteries, *EcoMat*, 2024, **6**, e12452, DOI: 10.1002/eom2.12452.

34 J. Meng, G. Jia, H. Yang and M. Wang, Recent advances for SEI of hard carbon anode in sodium-ion batteries: A mini review, *Front. Chem.*, 2022, **10**, 986541, DOI: 10.3389/fchem.2022.986541.

35 Y. Zhang, B. Wu, J. Bi, X. Zhang, D. Mu, X.-Y. Zhang, L. Zhang, Y. Xiao and F. Wu, Facilitating prelithiation of silicon carbon anode by localized high-concentration electrolyte for high-rate and long-cycle lithium storage, *Carbon Energy*, 2024, **6**, e480, DOI: 10.1002/cey2.480.

36 X. Zhang, H. Qu, W. Ji, D. Zheng, T. Ding, C. Abegglen, D. Qiu and D. Qu, Fast and Controllable Prelithiation of Hard Carbon Anodes for Lithium-Ion Batteries, *ACS Appl. Mater. Interfaces*, 2020, **12**, 11589–11599, DOI: 10.1021/acsami.9b21417.

37 N. Ren, L. Wang, X. He, L. Zhang, J. Dong, F. Chen, J. Xiao, B. Pan and C. Chen, High ICE Hard Carbon Anodes for Lithium-Ion Batteries Enabled by a High Work Function,

ACS Appl. Mater. Interfaces, 2021, **13**, 46813–46820, DOI: 10.1021/acsami.1c14935.

38 P.-H. Chang and C. A. Wilkie, A mechanism for flame retardation of poly(ethylene terephthalate), *J. Appl. Polym. Sci.*, 1989, **38**, 2245–2252, DOI: 10.1002/app.1989.070381208.

39 T. Ungár, Microstructural parameters from X-ray diffraction peak broadening, *Scr. Mater.*, 2004, **51**, 777–781, DOI: 10.1016/j.scriptamat.2004.05.007.

40 P. Wang, X. Zhu, Q. Wang, X. Xu, X. Zhou and J. Bao, Kelp-derived hard carbons as advanced anode materials for sodium-ion batteries, *J. Mater. Chem. A*, 2017, **5**, 5761–5769, DOI: 10.1039/C7TA00639J.

41 A. C. Ferrari, Interpretation of Raman spectra of disordered and amorphous carbon, *Phys. Rev. B: Condens. Matter Mater. Phys.*, 2000, **61**, 14095–14107, DOI: 10.1103/PhysRevB.61.14095.

42 P. B. Naik, N. S. Reddy, S. K. Nataraj, U. N. Maiti, H. K. Beere, P. Thippeswamy, H. Y. Jung and D. Ghosh, Optimizing Hard Carbon Anodes from Agricultural Biomass for Superior Lithium and Sodium Ion Battery Performance, *ChemSusChem*, 2025, **18**, e202400970, DOI: 10.1002/cssc.202400970.

43 S. Wu, H. Peng, L. Huang, Y. Liu, Y. Wu, L. Liu, W. Ai and Z. Sun, P-doped hard carbon microspheres for sodium-ion battery anodes with superior rate and cyclic performance, *Inorg. Chem. Front.*, 2023, **10**, 5908–5916, DOI: 10.1039/D3QI01296D.

44 J. Zheng, T. Cao, B. Ding, X. Zhang, H. Wu and X. Li, Facile synthesis of N, P co-doped carbon materials derived from corn bract for high-performance symmetric supercapacitors, *J. Energy Storage*, 2025, **110**, 115297, DOI: 10.1016/j.est.2025.115297.

45 J. Song, S. Jiang, Y. Wang, Y. Meng, D. Xiao, Q. Zhao, X. Zhang and B. He, Synergistic effects of P-functionalization and localized graphitization in sustainable hard carbon for enhanced sodium and potassium storage, *J. Colloid Interface Sci.*, 2025, **686**, 1200–1214, DOI: 10.1016/j.jcis.2025.02.028.

46 Z. Yang, Y. Gao, Z. Zhao, Y. Wang, Y. Wu and X. Wang, Phytic acid assisted formation of P-doped hard carbon anode with enhanced capacity and rate capability for lithium ion capacitors, *J. Power Sources*, 2020, **474**, 228500, DOI: 10.1016/j.jpowsour.2020.228500.

47 L. Xie, C. Tang, Z. Bi, M. Song, Y. Fan, C. Yan, X. Li, F. Su, Q. Zhang and C. Chen, Hard Carbon Anodes for Next-Generation Li-Ion Batteries: Review and Perspective, *Adv. Energy Mater.*, 2021, **11**, 2101650, DOI: 10.1002/aenm.202101650.

48 J. Wang, Y. Xia, Y. Liu, W. Li and D. Zhao, Mass production of large-pore phosphorus-doped mesoporous carbon for fast-rechargeable lithium-ion batteries, *Energy Storage Mater.*, 2019, **22**, 147–153, DOI: 10.1016/j.ensm.2019.01.008.

49 M. E. Suss, T. F. Baumann, M. A. Worsley, K. A. Rose, T. F. Jaramillo, M. Stadermann and J. G. Santiago, Impedance-based study of capacitive porous carbon electrodes with hierarchical and bimodal porosity, *J. Power Sources*, 2013, **241**, 266–273, DOI: 10.1016/j.jpowsour.2013.03.178.

50 R. Kant and M. B. Singh, Theory of the Electrochemical Impedance of Mesostructured Electrodes Embedded with Heterogeneous Micropores, *J. Phys. Chem. C*, 2017, **121**, 7164–7174, DOI: 10.1021/acs.jpcc.7b01287.

51 D. Kang, H.-K. Kim, H.-J. Kim and Y. Han, Preparation of biomass-derived hard carbon with uniform ultramicropores for development of fast charging Li-ion batteries, *J. Alloys Compd.*, 2022, **900**, 163420, DOI: 10.1016/j.jallcom.2021.163420.

52 K. Wang, Y. Xu, H. Wu, R. Yuan, M. Zong, Y. Li, V. Dravid, W. Ai and J. Wu, A hybrid lithium storage mechanism of hard carbon enhances its performance as anodes for lithium-ion batteries, *Carbon*, 2021, **178**, 443–450, DOI: 10.1016/j.carbon.2020.11.095.

53 H.-Y. Yu, H.-J. Liang, Z.-Y. Gu, Y.-F. Meng, M. Yang, M.-X. Yu, C.-D. Zhao and X.-L. Wu, Waste-to-wealth: low-cost hard carbon anode derived from unburned charcoal with high capacity and long cycle life for sodium-ion/lithium-ion batteries, *Electrochim. Acta*, 2020, **361**, 137041, DOI: 10.1016/j.electacta.2020.137041.

54 M.-J. He, L.-Q. Xu, B. Feng, J.-B. Hu, S.-S. Chang, G.-G. Liu, Y. Liu and B.-H. Xu, Tannin-Derived Hard Carbon for Stable Lithium-Ion Anode, *Molecules*, 2022, **27**, 6994, DOI: 10.3390/molecules27206994.

55 Y. Xi, S. Huang, D. Yang, X. Qiu, H. Su, C. Yi and Q. Li, Hierarchical porous carbon derived from the gas-exfoliation activation of lignin for high-energy lithium-ion batteries, *Green Chem.*, 2020, **22**, 4321–4330, DOI: 10.1039/D0GC00945H.